**Proceedings of the ASME 2020 39th International Conference on Ocean, Offshore and Arctic Engineering**
**OMAE 2020**
**June 28-July 3, 2020, Fort Lauderdale, FL, USA**

**OMAE2020-18501**

# A FLUID-STRUCTURE COUPLED COMPUTATIONAL MODEL FOR THE CERTIFICATION OF SHOCK-RESISTANT ELASTOMER COATINGS

**Wentao Ma, Xuning Zhao, Kevin Wang***
Department of Aerospace and Ocean Engineering
Virginia Polytechnic Institute and State University
Blacksburg, Virginia 24061

## ABSTRACT

*Shock waves from underwater and air explosions are significant threats to surface and underwater vehicles and structures. Recent studies on the mechanical and thermal properties of various phase-separated elastomers indicate the possibility of applying these materials as a coating to mitigate shock-induced structural failures. To demonstrate this approach and investigate its efficacy, this paper presents a fluid-structure coupled computational model capable of predicting the dynamic response of air-backed bilayer (i.e. elastomer coating – metal substrate) structures submerged in water to hydrostatic and underwater explosion loads. The model couples a three-dimensional multiphase finite volume computational fluid dynamics model with a nonlinear finite element computational solid dynamics model using the FIVER (FInite Volume method with Exact multi-material Riemann solvers) method. The kinematic boundary condition at the fluid-structure interface is enforced using an embedded boundary method that is capable of handling large structural deformation and topological changes. The dynamic interface condition is enforced by formulating and solving local, one-dimensional fluid-solid Riemann problems, which is well-suited for transferring shock and impulsive loads. The capability of this computational model is demonstrated through a numerical investigation of hydrostatic and shock-induced collapse of aluminum tubes with polyurea coating on its inner surface. The thickness of the structure is resolved explicitly by the finite element mesh. The nonlinear material behavior of polyurea is accounted for using a hyper-viscoelastic constitutive model featuring a modified Mooney-Rivlin equation and a stress relaxation function in the form of prony series. Three numerical experiments are conducted to simulate and compare the collapse of the structure in different loading conditions, including a constant pressure, a fluid environment initially in hydrostatic equilibrium, and a two-phase fluid flow created by a near-field underwater explosion.*

## INTRODUCTION

Shock waves from underwater and air explosions are major threats to ocean vehicles and structures. The design and application of shock mitigation materials and methods has been a long-standing active research area. Within this area, recent studies have revealed some extraordinary properties of several phase-separated elastomers (e.g., polyureas), which indicates a promising approach for mitigating shock-induced damage and failure [1–5]. Specifically, these copolymers with separated glassy and rubbery domains at nm to μm scales can be tailored chemically to achieve a combination of energy dissipation, resilience, and stiffness under high pressure, high strain-rate loading. Therefore, they can be applied to the surface of various structures as a shock (and ballistic impact) mitigation coating.

As an example, the effectiveness of polyurea coatings for mitigating shock-induced deformation and fracture has been demonstrated at different scales (e.g., [1, 6, 7]). These studies have also shown that the performance of the coating under shock loading depends not only on their material properties, but also on

*Corresponding author. E-mail address: kevinwgy@vt.edu

the complex dynamic interaction of the coating material with the underlying substrate and the surrounding fluid media (e.g., water, air). For example, it has been shown that the effectiveness of the coating depends on the material of the substrate, and on which side of it (i.e. inner or outer surface) the coating is applied [7]. Also, the effect of the same polyurea coating under underwater and aerial shock loadings are different [7]. Furthermore, it has been found that increasing the coating thickness continuously does not translate to a continuous increase in its performance, and the optimal thickness depends sensitively on both the shock loading condition and the substrate [1].

Because of these complexities, the design and practical use of high strain-rate sensitive elastomer coatings for specific engineering applications require improved knowledge and predictive capability regarding a challenging shock-dominated multi-material fluid-structure interaction problem, featuring

- three-dimensional (3D) shock wave transmission, reflection, and attenuation through the solid and fluid materials and at their interfaces (i.e. fluid-coating, coating-substrate, and substrate-fluid interfaces);
- large deformation, hyper-elastic, and viscoelastic/viscoplastic behaviors of the coating material; and
- shock-induced material damage and dynamic fracture under high strain-rate loading.

In the past, extensive research has been devoted towards understanding the mechanical behaviors of elastomer coatings under high pressure, high strain-rate loading (e.g., [1, 4–16]). Several fundamental mechanisms by which elastomer coatings protect the substrate have been identified through laboratory experiments (e.g., Barsoum and Dudt [1], Amini *et al.* [6]) and numerical analysis (e.g., Heyden *et al.* [8], Filonova *et al.* [9]). Several research teams have tested elastomer material coupons to measure their properties and dynamics under high strain-rate and high pressure loading. For example, using a high-speed drop weight tensile test instrument, Roland *et al.* [5] carried out stress-strain measurements for polyureas with strain rate varying from $10^{-2}$ $s^{-1}$ to $10^{2}$ $s^{-1}$. Using the Split-Hopkinson Pressure Bar with various modifications, a few teams (e.g., Yi *et al.* [10], *Sarva et al.* [11], Song *et al.* [12], Nemat-Nasser *et al.* [13]) have conducted compression tests for polyureas (and other elastomers) with strain rate varying from $10^{2}$ $s^{-1}$ to $10^{3}$ $s^{-1}$. It has been discovered that as strain rate increases to $10^{3}$ $s^{-1}$, its elastic modulus can increase by up to three orders of magnitude. Using a sandwiched Pressure-Shear Plate Impact (PSPI) facility, Jiao *et al.* [4, 14] have conducted pressure-shear tests on polyurea, and found that at a strain rate of $10^{5}$ to $10^{6}$ $s^{-1}$, the response (e.g., shear resistance, shear wave speed) of polyurea also depends sensitively on the impact pressure. For example, they found that when the impact pressure increases from 1 to 10 GPa, the plateau-level (saturation) shear resistance of polyurea P-1000 increases also by one order of magnitude, from 0.1 GPa to 1.0 GPa.

These studies have shown that the response of elastomeric polyurea under high pressure and high strain-rate loading, such as in the scenarios of underwater and aerial explosions, is closely related to the material's highly nonlinear properties and behaviors, including (1) large strain nonlinear elasticity, (2) asymmetric stress-strain behavior in compression and tension, (3) rate- and pressure-dependent viscoelasticity and viscoplasticity, (4) substantial hysteresis during unloading, and (5) stretch-induced softening [7, 17]. Based on the experimental data obtained, several constitutive models have been developed and calibrated to account for these features. For example, Amirkhizi *et al.* [18] developed and calibrated a viscoelastic constitutive model for polyurea, where the viscoelastic relaxation is modeled using a 4-term Prony series, which is then scaled to account for the impacts of temperature and pressure. Cho *et al.* [17] developed and calibrated a viscoelastic-viscoplastic constitutive model for polyurea (PU1000), in which the nonlinear strain-rate dependence is captured using separate micro-rheological linear spring-and-dashpot models for the soft (rubbery) and hard (glassy) domains of polyurea. Clifton *et al.* [19] have developed and calibrated a quasi-linear viscoelastic constitutive model for polyurea, featuring a continuous distribution of viscoelastic relaxation times. The model also generalizes the Mooney-Rivlin hyperelasticity model with an additional multiplicative factor that accounts for the (experimentally observed) dependence of shear wave speed on pressure.

Despite the recent progresses reviewed above, the dynamic process of shock wave impacting on the bilayer coating-substrate structure is still unclear, which involves the propagation and attenuation of shock waves within multiple solid (elastomer coating and substrate) and fluid (e.g., water, air) materials, as well as the dynamic interaction of these materials at fluid-structure and coating-substrate interfaces. In this paper, we present a three-dimensional CFD (computational fluid dynamics) – CSD (computational solid dynamics) coupled computational model, referred to as FIVER (FInite Volume method with Exact multi-material Riemann solvers), for predicting the dynamic response of bilayer elastomer coating – substrate systems (e.g., polyurea-aluminum) to underwater shock loading. The key components of FIVER relevant to this study include (1) a parallel nonlinear (both material-wise and geometry-wise) finite element CSD solver, equipped with a modified Mooney-Rivlin hyperelasticity model [19] and a prony series viscoelastic relaxation function [18] for polyurea, (2) a parallel finite volume, multiphase compressible Navier-Stokes CFD solver, equipped with a level-set method for tracking fluid-fluid interfaces (e.g., UNDEX bubble) [20, 21]; (3) a second-order, numerically stable partitioned time-integrators for coupling the CFD and CSD solvers [22]; and (4)a second-order embedded boundary method with multi-material Riemann problem solvers for enforcing the transmission conditions at fluid-structures interfaces, particularly designed for

problems involving large deformation and fracture [20, 23–28]. Over the past decade, FIVER has been applied to study several fluid-structure interaction problems in ocean, aerospace, and biomedical engineering applications, including underwater hydrostatic implosion [29, 30], pipeline explosion [31, 32], shock wave lithotripsy [33–35], bio-mimetic propulsors [36], and supersonic parachute deployment [37].

We demonstrate the computational model through a numerical investigation of hydrostatic and shock-induced collapse of an aluminum cylinder with polyurea coating on its inner surface. The thickness of the structure is resolved explicitly by the finite element mesh. The nonlinear material behavior of polyurea is accounted for using a hyper-viscoelastic constitutive model featuring a modified Mooney-Rivlin equation [19] and a stress relaxation function in the form of prony series [18]. Three numerical tests are presented, in which the structure is subjected to different loading conditions, including a constant pressure (i.e. without consideration of fluid-structure interaction), an ambient fluid initially at rest, and a two-phase fluid flow created by a near-field underwater explosion.

## PHYSICAL MODEL AND NUMERICAL METHODS

We consider a model problem shown in Figure 1, which involves a cylindrical metal structure submerged in water. The elastomer coating can be applied on either side of the metal. This figure illustrates the secenario of a near-field explosion, that is, the distance between the explosive charge and the structure is relatively small, such that the dynamics of the gaseous explosion product — sometimes referred to as the "bubble" — should also be considered. Therefore, the problem involves three fluid subdomains: the ambient fluid (i.e. water), the gas inside the structure (e.g., air), and the explosion product. If instead the explosion occurs at a large distance from the structure, it can be modeled as a pressure wave, with profile and amplitude determined by experimental data and similitude equations (cf. [38, 39]).

Due to the presence of shock waves, the fluid in all the subdomains are modeled as compressible flows, governed by the Navier-Stokes equations,

$$\frac{\partial W(x,t)}{\partial t} + \nabla \cdot F(W) = \nabla \cdot G(W, \nabla W), \tag{1}$$

with

$$W = \begin{bmatrix} \rho \\ \rho V \\ \rho e_t \end{bmatrix}, \quad F = \begin{bmatrix} \rho V^T \\ \rho V \otimes V + p\boldsymbol{I} \\ (\rho e_t + p)V^T \end{bmatrix}, \quad G = \begin{bmatrix} 0 \\ \boldsymbol{\tau} \\ V^T\boldsymbol{\tau} - Q^T \end{bmatrix}, \tag{2}$$

where we have used lower case, upper case, and bold letters to denote scalars, vectors, and second-order tensors, respectively.

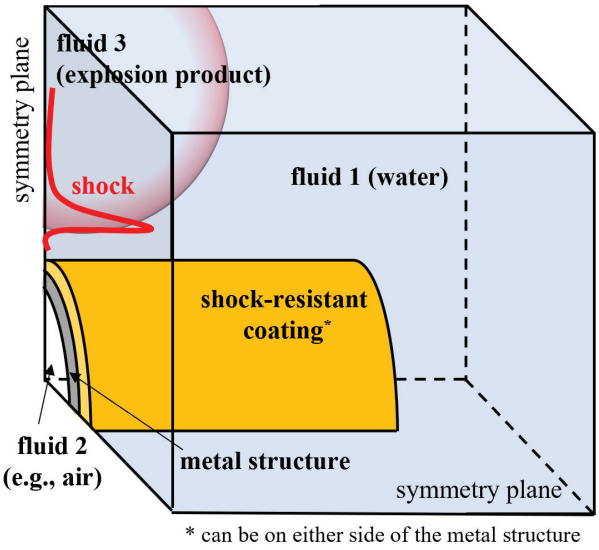


**FIGURE 1**: Certification of shock-resistant elastomer coatings: A model problem.

Specifically, $\rho$, $V$, $e_t$, $p$, and $\boldsymbol{\tau}$ denote fluid density, velocity, total energy per unit mass, pressure, and the viscous stress tensor, respectively. $\boldsymbol{I}$ is the $3 \times 3$ identity matrix. $Q$ denotes the heat flux. Equations (1) and (2) have already neglected any body forces (in particular, gravity) and heat sources. In this paper, for simplicity we also neglect the effects of viscosity and heat diffusion, which reduces Equation (1) to the Euler equations, i.e.

$$\frac{\partial W(x,t)}{\partial t} + \nabla \cdot F(W) = 0, \tag{3}$$

Following Wang *et al.* [31], we adopt the Tait equation of state (EOS) for the liquid water, and the perfect gas EOS for the gas inside the cylinder. For simplicity, in this paper we model the gaseous explosion product as a high pressure air bubble, also using the perfect gas EOS. The level-set equation is solved to track the evolution of the bubble.

To solve the multi-material fluid-structure interaction problem, we apply the method of FIVER (Finite Volume method with Exact multi-material Riemann solvers). In an augmented fluid domain that includes all the fluid subdomains and the region occupied by the solid structure, the fluid governing equations are semi-discretized by an unstructured, node centered, non-interface-conforming finite volume mesh. Then, for an arbitrary control volume $C_i$, the Euler equations are integrated, which gives

$$\frac{\partial W_i}{\partial t} + \frac{1}{\|C_i\|} \sum_{j \in N(i)} \int_{\partial C_{ij}} F(W) \cdot \boldsymbol{n}_{ij} dS = 0, \tag{4}$$

where $W_i$ denotes the average $W$ in control volume $C_i$; $\|C_i\|$ denotes the volume of $C_i$; $N(i)$ is the set of nodes that are connected to node i by an edge; $\partial C_{ij} = \partial C_i \cap \partial C_j$ is the boundary faces of the two control volume; and $\boldsymbol{n}_{ij}$ is the unit normal to $\partial C_{ij}$. Then, we compute the flux in different ways, depending on the location of nodes $i$ and $j$ — specifically, which fluid or structural subdomain does it belong to. Additional details of FIVER have been presented in previous publications, including [26, 27, 31].

The dynamic equilibrium of a structure undergoing finite deformation is modeled in the Lagrangian setting using the following equations

$$\rho_s \frac{\partial^2 u_j}{\partial t^2} = \frac{\partial}{\partial x_i}\left(\tau_{ij} + \tau_{im}\frac{\partial u_j}{\partial x_m}\right) + b_j, \tag{5}$$

where the subscripts $i$, $j$, and $m$ vary from 1 to 3 and designate the $(x, y, z)$ coordinate system. $\rho_s$ denotes structure density in the undeformed configuration, $u$ the displacement vector, and $\tau$ the second Piola–Kirchoff stress tensor[1]. $b$ denotes the body force vector, which is set to 0 in this paper. The dynamic response of polyurea is modeled as an instantaneous elastic response followed by a viscoelastic stress relaxation process. Accordingly, the constitutive model for polyurea consists of two parts, namely a hyperelastic model and a stress relaxation model.

When modeling the instantaneous elastic response, polyurea is considered as an isotropic hyperelastic material undergoing finite deformation. The hyperelastic model used in this paper is the one proposed by Clifton *et al.* [19]. In this model, the strain energy density function has the form

$$\bar{W} = f(J)\hat{W}(\bar{I}_1, \bar{I}_2), \tag{6}$$

where $\hat{W}(\bar{I}_1, \bar{I}_2)$ is the strain energy associated with distortion, and $f(J)$ is a factor that depicts the effect of volumetric change. This multiplicative decomposition of strain energy, in contrast to the traditional addictive decomposition, was designed to better describe the shear wave speed's strong dependence on pressure.

Following Clifton *et al.* [19], the factor $f(J)$ takes the form

$$f(J) = \left(J^{-M} - 2J^{-N}\right) + 2, \tag{7}$$

where $J$ is the volume ratio after and before deformation. It can be computed as the square root of the determinant of right Cauchy-Green deformation tensor. $M$ and $N$ are material constants, and $M = 2N$. The "+2" in Equation (7) allows $f(J)$ to satisfy the requirement of $f(1) = 1$.

The distortional strain energy, $\hat{W}(\bar{I}_1, \bar{I}_2)$, has the Mooney Rivlin form,

$$\hat{W}(\bar{I}_1, \bar{I}_2) = C_{00} + C_{01}(\bar{I}_2 - 3) + C_{02}(\bar{I}_1 - 3), \tag{8}$$

where $\bar{I}_1$ and $\bar{I}_2$ are given by

$$\bar{I}_1 = J^{-2/3} I_1, \tag{9}$$

$$\bar{I}_2 = J^{-4/3} I_2, \tag{10}$$

where $I_1$ and $I_2$ are the first and second invariant of the right Cauchy-Green deformation tensor.

The right Cauchy-Green deformation tensor, $C$, has the following relation with the Green-Lagrangian strain tensor $E$:

$$\boldsymbol{C} = 2\boldsymbol{E} + \boldsymbol{I}, \tag{11}$$

where $I$ is the $3 \times 3$ identity matrix.

The second Piola–Kirchoff stress tensor $\boldsymbol{\tau}$ is given by

$$\boldsymbol{\tau} = \frac{\partial \bar{W}}{\partial \boldsymbol{E}}, \tag{12}$$

and the Cauchy stress tensor $T$ is given by

$$T = \frac{1}{\det(\boldsymbol{F})}\boldsymbol{F}\boldsymbol{\tau}\boldsymbol{F}^T, \tag{13}$$

where $F$ is the deformation gradient tensor.

The stress relaxation model addresses the deviatoric and the hydrostatic (dilatational) stress components in different ways. The reason is that, in many cases, the dilatational response of polyurea can be effectively modeled as elastic. Amirkhizi *et al.* [18] and Clifton and Jiao [7] also showed that the effect of hydrostatic stress relaxation is small. Therefore, in this work, the viscoelastic stress relaxation process is only applied to deviatoric stresses. The deviatoric and hydrostatic parts of the instantaneous Cauchy stresses have the relation given by

$$\sigma^e_{ij} = T_{ij} - \sigma^e_{\text{hyd}}\delta_{ij}, \tag{14}$$

where $\sigma^e_{ij}$ is the instantaneous elastic deviatoric stress, $T_{ij}$ is the instantaneous elastic Cauchy stress, $\delta_{ij}$ is the Kronecker delta, and $\sigma^e_{\text{hyd}}$ is the hydrostatic stress, given by

$$\sigma^e_{\text{hyd}} = \frac{\text{tr}(\boldsymbol{T})}{3}, \tag{15}$$

where tr denotes the trace operator.

The deviatoric stress after relaxation, $\sigma(t)$, may be expressed in the form of the convolution integral as shown by Goh *et al.* [40], i.e.

$$\sigma(t) = \int_0^t g(t-s)\frac{d\sigma^e}{ds}ds, \tag{16}$$

[1] to be distinguished from the fluid viscous stress tensor.

where $g(t)$ is the relaxation function, which can be written in the form of Prony series,

$$g(t) = g_\infty + \sum_{i=1}^{N} g_i \exp\Big(-\frac{t}{\tau_i}\Big), \tag{17}$$

where $\tau_i$ (not the stress tensor) are relaxation times, $g_\infty$ and $g_i$ ($i = 1, \cdots, N$) are dimensionless constants.

$$g_\infty + \sum_{i=1}^{N} g_i = 1. \tag{18}$$

Substituting Equation (17) into (16) yields

$$\sigma(t) = g_\infty \sigma^e(t) + \sum_{i=1}^{N} g_i \int_0^t \exp\Big(-\frac{t-s}{\tau_i}\Big)\frac{d\sigma^e}{ds} ds. \tag{19}$$

One benefit of the exponential form in Equation (17) (the Prony series) is that the convolution integral can be evaluated using a finite time increment formulation which, instead of storing the entire stress history, only needs to store the information from last time step. Thus, the computational expense is significantly reduced.

Specifically, when implementing the stress relaxation model (in particular, Equation (19)), the following property of the exponential function is utilized:

$$\exp\Big(-\frac{t_{n+1}}{\tau_i}\Big) = \exp\Big(-\frac{t_n}{\tau_i}\Big)\exp\Big(-\frac{\Delta t}{\tau_i}\Big), \tag{20}$$

where the subscripts $n$ and $n+1$ denote two consecutive time steps, and $\Delta t$ the time step size.

Substituting Equation (20) into (19), we obtain the recursive formula

$$\begin{aligned}\sigma(t_{n+1}) = g_\infty \sigma^e(t_{n+1}) + \sum_{i=1}^{N} \Big( &\exp\big(-\frac{\Delta t}{\tau_i}\big) h_i(t_n) \\ &+ g_i \tau_i \frac{\sigma^e(t_{n+1}) - \sigma^e(t_n)}{\Delta t}\big(1 - \exp\big(-\frac{\Delta t}{\tau_i}\big)\big)\Big),\end{aligned} \tag{21}$$

where

$$h_i(t_n) = \int_0^t g_i \exp\big(-\frac{t-s}{\tau_i}\big)\frac{d\sigma^e}{ds} ds. \tag{22}$$

Using Equation (21), the computation of stress at any time step only requires information from the previous step. This is an important advantage as it simplifies implementation and significantly reduces memory requirement.

## NUMERICAL EXPERIMENTS

The structure investigated is a circular aluminum shell with polyurea coating applied on its inner surface. The axial thickness of the shell is 0.4 mm. The radius and the radial thickness of the aluminum shell are 19.1 mm and 0.711 mm, respectively. The radial thickness of polyurea coating is 0.2 mm. The entire structure is discretized with hexahedron grids. The aluminum shell and polyurea coating have 5 and 4 layers of grid in radial direction respectively. In circumferential direction, the structure is divided into 400 elements. Since there is no force or motion in axial direction (i.e. the $x$-axis), only one layer of grid is used in axial direction. Figure 1 (top) shows the geometry and the finite element grid of the structural model, including both the aluminum shell and the polyurea coating.

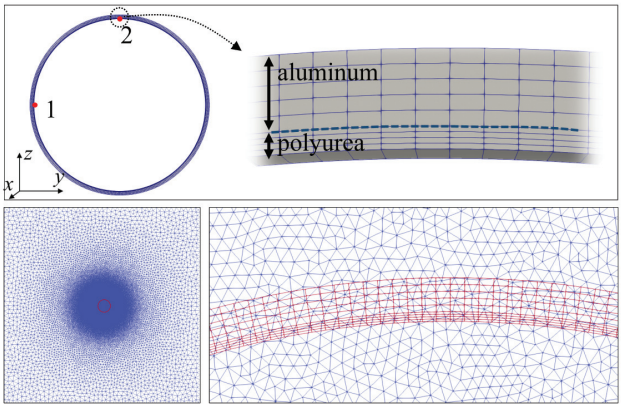


**FIGURE 2**: Setup of numerical experiment: A finite element model of an aluminum cylinder coated with polyurea on its inner surface (top), and an unstructured, non-interface-conforming finite volume fluid mesh for fluid-structure coupled analysis (bottom).

In the numerical experiments, aluminum has a Young's modulues of 70.8 GPa, Poisson's ratio of 0.33, and a density of $2.78 \times 10^{-3}$ g/mm$^3$. The constitutive model of the aluminum shell is a finite strain plastic material law, in which the yielding stress is 30.4 GPa, tangent modulus is 66.74 GPa, and the hardening is pure isotropic. The constitutive models of polyurea coating have been discussed in the previous section. The parameters in hyperelasticity model are identical to those in Clifton *et al.* [19]: density is $1.07 \times 10^{-3}$g/mm$^3$, $C_{00} = 0.2684$ GPa, $C_{01} = C_{02} = 0.1098$ GPa, and $M = 4.4$. The stress relaxation model uses a two-term Proney series, in which the parameters are acquired through simplifying the four-term Proney series from Amirkhizi *et al.* [18]. Based on the time scale of the current problem (of the order of milliseconds), we adopt the two terms in the relaxation function with $\tau = 0.064$ ms and $1.163 \times 10^{-4}$ ms.

Therefore, the parameters are $g_\infty = 0.26$, $g_1 = 0.237$, $g_2 = 0.503$, $\tau_1 = 0.064$ ms, and $\tau_2 = 1.163 \times 10^{-4}$ ms. In the structural model, a 0.1% ovality is introduced as a geometric imperfection to drive the structure to collapse in mode 2.

Figure 2 also shows a top view of the unstructured non-interface-conforming fluid mesh, which has 0.21 million nodes and 0.64 million tetrahedron elements. In the most refined region, that is, where the structure and the bubble are located, the characteristic element size is 0.3 mm.

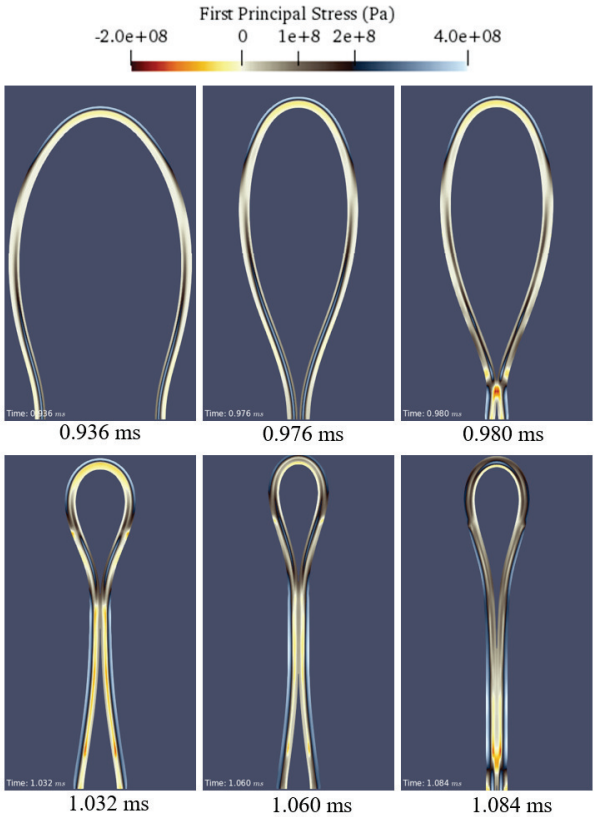


**FIGURE 3**: Collapse of the aluminum-polyurea structure under a constant pressure load. (The upper half of the structure is shown.)

Next, we present three numerical tests in which the structure is placed in different loading conditions. Specifically, we present

- a "dry" simulation in which the outer surface of the structure is subjected to a constant pressure, 1.8 MPa. As the structure deforms, the direction of the pressure load at any point changes accordingly (as a follower force). Nonetheless, the magnitude of pressure is fixed. This setup effectively decouples the dynamics of the structure from that of the surrounding fluid. Therefore, the fluid dynamics solver is not involved in the simulation.
- A fluid-structure coupled analysis of the collapse of the structure due to hydrostatic pressure. In this case, the fluid pressure is initially set to 1.8 MPa, in consistency with the dry simulation.
- A fluid-structure coupled analysis of the a near-field explosion. The explosion bubble is modeled as a spherical bubble with an initial radius of 2.5 mm, centered at approximately 11 mm from the outer surface of the structure. The pressure and density inside the bubble are set to 50.0 MPa and $5.0 \times 10^{-5}$ g/mm$^3$. The hydrostatic pressure is set to 1.0 MPa, which is lower than the (hydrostatic) collapse pressure of the structure.

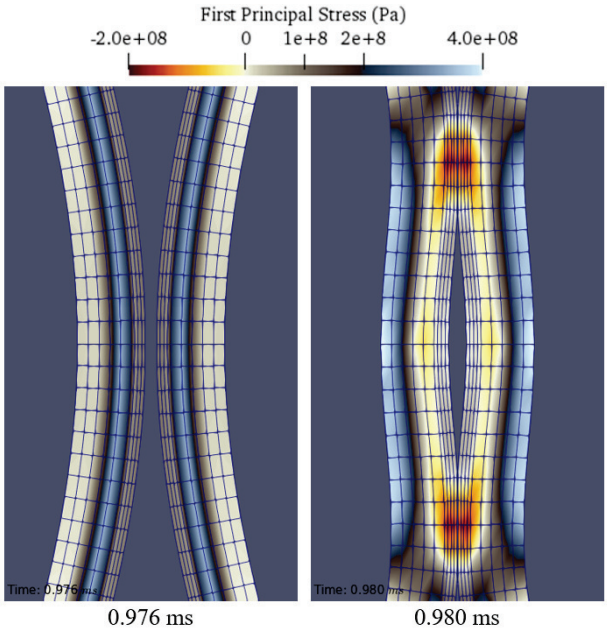


**FIGURE 4**: A close-up view of the self-contact.

Figures 3 and 4 present the time-history of the structural deformation and stress predicted by the dry simulation, with Figure 4 showing the moment of self-contact. The process of collapse takes about 0.98 ms until the middle points (in $z$-axis) reach in contact. Afterwards, the region of contact moves towards the upper and lower ends, until approximately 1.08 ms, the structure is roughly in static equilibrium (but still with high frequency, low amplitude oscillations).

Figures 5 and 6 present the time-history of fluid pressure and structural dynamics predicted by the second simulation, which accounts for the fluid-structure interaction during the collapse of the structure. As the boundary of the structure moves inward, it gives the surrounding water a non-zero velocity, which leads

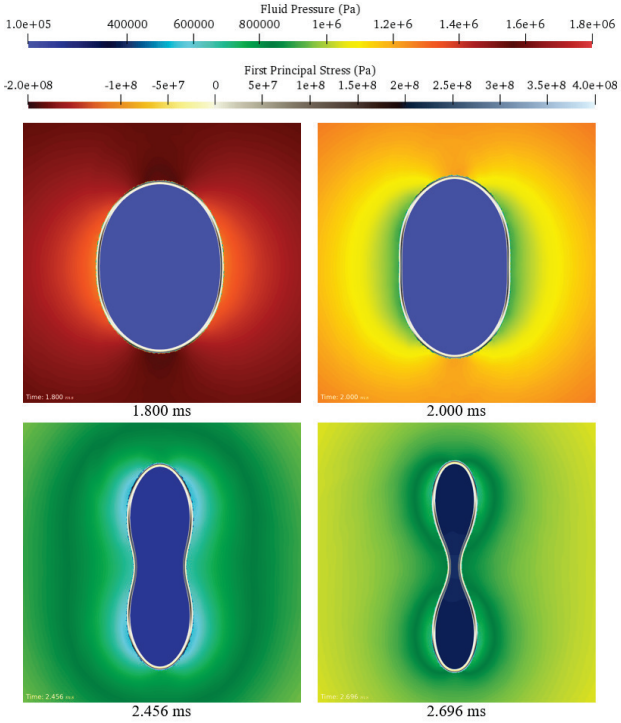


**FIGURE 5**: Fluid-structure coupled analysis of collapse due to hydrostatic pressure: Time-history of fluid and structural results, before the structure reaches self-contact.

to the reduction of pressure. This in turn reduces the pressure load on the structural surface, thereby decreasing the speed of its collapse. Figure 6 presents a sequence of images showing the pressure variation after the structure reaches self-contact. To the surrounding fluid flow, the contact of the structure means a sudden drop of velocity (to approximately 0), which leads to a sudden rise of pressure. Figure 6 shows that as the region of contact spreads out, the region of high pressure follows its front.

Comparing the results obtained from the dry and coupled simulations, it is clear that the former significantly overpredicts the speed of the structure's collapse, as it ignores the decrease of pressure in the surrounding flow during the course. Figure 7 compares the local displacement at two sensors on the inner surface of the structure (i.e. in the region of polyurea). The time of collapse, measured up to the time instance the structure reaches self-contact, is found to be 0.98 ms in the dry simulation, compared to 2.7 ms in the coupled simulation. In addition, Figure 8 compares the structural velocity at one of the two sensors. It can be observed that in both the dry and the coupled simulations, the velocity increases monotonically throughout the duration of the collapse. The maximum velocity is found to be around 125 m/s in the dry simulation, which is about 6 times higher than that in the coupled simulation.

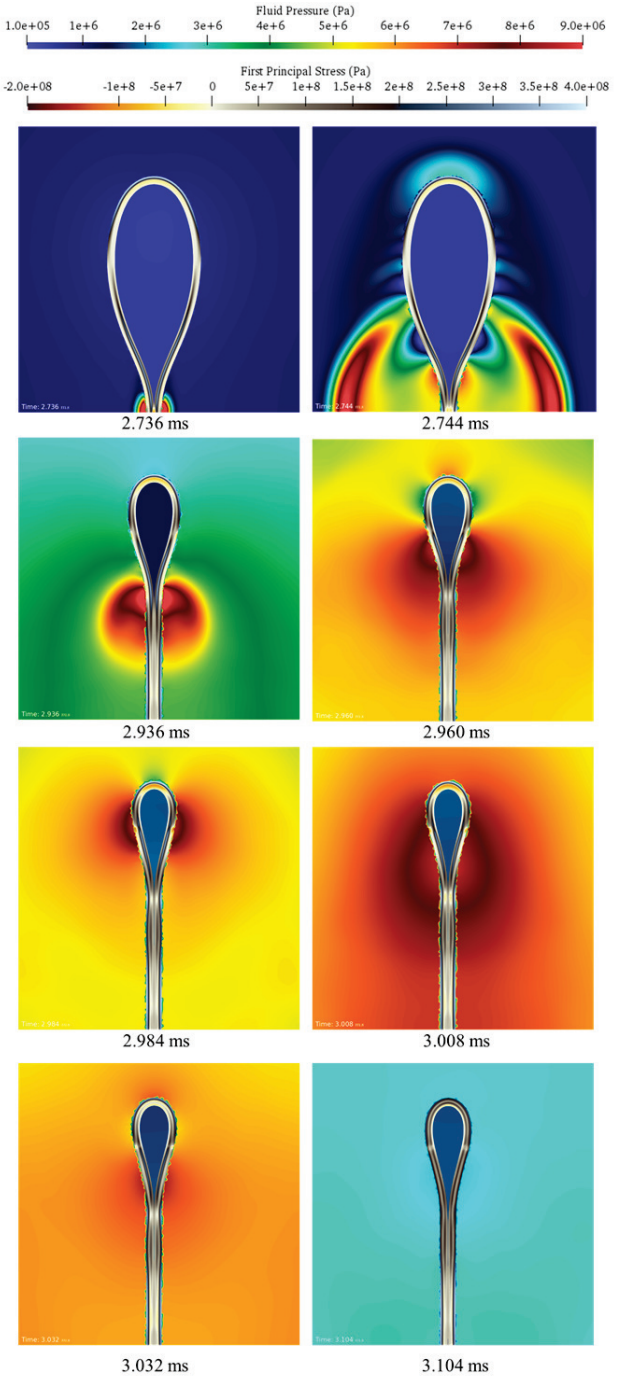


**FIGURE 6**: Fluid-structure coupled analysis of collapse due to hydrostatic pressure: Time-history of fluid and structural results after the structure reaches self-contact. (The upper half of the structure is shown.)

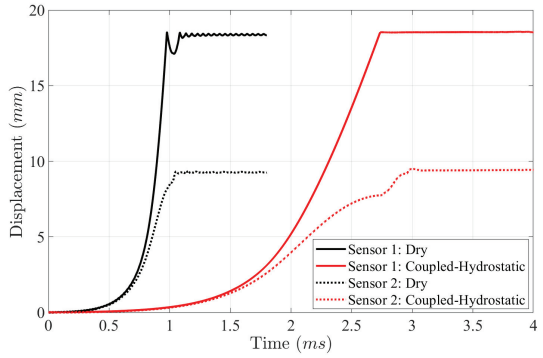


**FIGURE 7**: Comparison of "dry" and coupled analysis: Time-history of displacement at two sensor points on the inner surface of the structure (see Fig. 2).

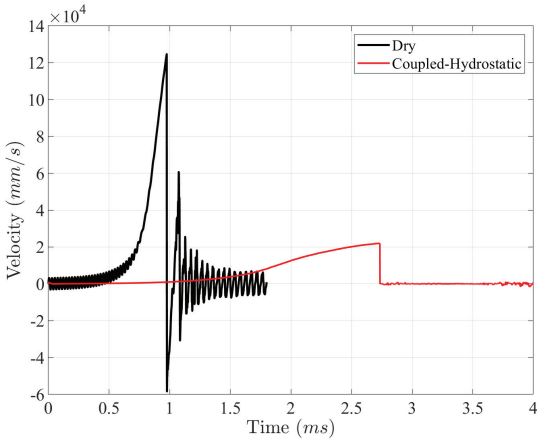


**FIGURE 8**: Comparison of "dry" and coupled analysis: Time-history of velocity at a sensor point on the inner surface of the structure (see Fig. 2).

Figure 9 shows a sequence of solution snapshots obtained from the third test, which features a near-field explosion. Specifically, the two images taken at 0.008 ms shows the spherical shock wave impacting on the top of the structure, which drives the structure to collapse. The structure's deformation is different from, and more complex than, that observed in the previous two test cases. At 0.3 ms, the upper side of the structure is moving inward, whereas the lower side is moving outward. As the upper side of the structure moves inward, it also pulls the bubble towards it. Gradually the bubble deforms from a perfect sphere to an oval. Between 0.3 ms and 2.1 ms, it can be observed that the structure vibrates instead of immediately flattens as found in the previous two cases. Interestingly, as the upper side of the structure bounces back (from 1.1 ms to 1.7 ms), it produces a liquid jet that penetrates into the bubble. As the jet moves inside the bubble, it generates two vortices, and gradually deforms into a mushroom shape. The last two columns of image, taken at 2.164 ms and 2.2 ms, shows that when the liquid jet reaches the upper side of the bubble, it leads to a sudden increase of pressure at the point of contact.

## Concluding Remarks

By adopting and implementing several recently developed constitutive models of polyurea, we have extended the FIVER framework to model and simulate the dynamic response of structures with polyurea coating to hydrostatic and underwater explosion loads. We have presented a numerical experiment that compares the response of a coated aluminum cylinder in different loading conditions, which also demonstrates the capabilities of the computational framework. Additional studies are being performed to validate the computational model, and applying it to simulate more realistic structures and test cases.

## ACKNOWLEDGMENT

The authors gratefully acknowledge the support of the Office of Naval Research (ONR) under Awards N00014-19-1-2102, and the support of the National Science Foundation (NSF) under Awards CBET-1751487.

## REFERENCES

[1] GS Barsoum and PJ Dudt. The fascinating behaviors of ordinary materials under dynamic conditions. *Ammtiac Quarterly*, 4:11–14, 2010.

[2] AD Mulliken and MC Boyce. Mechanics of the rate-dependent elastic–plastic deformation of glassy polymers from low to high strain rates. *International journal of solids and structures*, 43(5):1331–1356, 2006.

[3] Taeyi Choi, Daniel Fragiadakis, C Michael Roland, and James Runt. Microstructure and segmental dynamics of polyurea under uniaxial deformation. *Macromolecules*, 45(8):3581–3589, 2012.

[4] T Jiao and RJ Clifton. Measurement of the response of an elastomer at pressures up to 9 gpa and shear-rates of 105–106s- 1. In *Journal of Physics: Conference Series*, volume 500, page 112036. IOP Publishing, 2014.

[5] CM Roland, JN Twigg, Y Vu, and PH Mott. High strain rate mechanical behavior of polyurea. *Polymer*, 48(2):574–578, 2007.

[6] MR Amini, J Isaacs, and S Nemat-Nasser. Investigation of effect of polyurea on response of steel plates to impulsive loads in direct pressure-pulse experiments. *Mechanics of Materials*, 42(6):628–639, 2010.

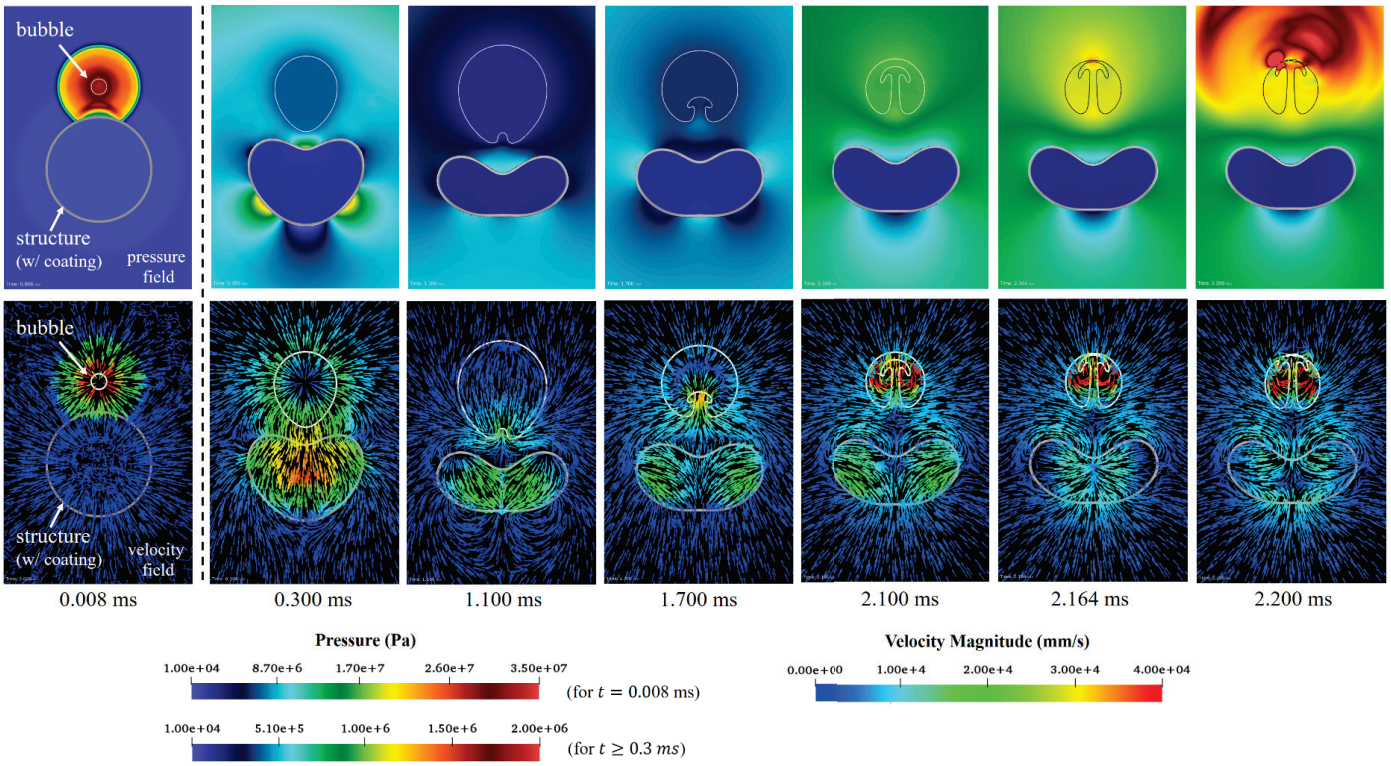


**FIGURE 9**: Result of the fluid-structure coupled analysis of a near-field explosion.


[7] Roshdy George S Barsoum. *Elastomeric Polymers with High Rate Sensitivity: Applications in Blast, Shockwave, and Penetration Mechanics*. William Andrew, 2015.

[8] Stefanie Heyden, B Li, Kerstin Weinberg, Sergio Conti, and M Ortiz. A micromechanical damage and fracture model for polymers based on fractional strain-gradient elasticity. *Journal of the Mechanics and Physics of Solids*, 74:175–195, 2015.

[9] Vasilina Filonova, Yang Liu, and Jacob Fish. Generalized viscoplasticity based on overstress (gvbo) for large strain single-scale and multiscale analyses. In *Numerical Simulations of Coupled Problems in Engineering*, pages 3–27. Springer, 2014.

[10] J Yi, MC Boyce, GF Lee, and E Balizer. Large deformation rate-dependent stress–strain behavior of polyurea and polyurethanes. *Polymer*, 47(1):319–329, 2006.

[11] Sai S Sarva, Stephanie Deschanel, Mary C Boyce, and Weinong Chen. Stress–strain behavior of a polyurea and a polyurethane from low to high strain rates. *Polymer*, 48(8):2208–2213, 2007.

[12] B Song and W Chen. Dynamic compressive behavior of epdm rubber under nearly uniaxial strain conditions. *J. Eng. Mater. Technol.*, 126(2):213–217, 2004.

[13] S Nemat-Nasser. Experimental characterization of polyurea with constitutive modeling and simulation. In *Proceedings of ONR, ERC, ACTD Workshop, MIT, Cambridge, Massachusetts*, 2004.

[14] Tong Jiao and Rodney Clifton. Experimental and computational investigation of the shearing resistance of an elastomer at pressures up to 18 gpa and strain rates of 105-106s-1. In *APS Shock Compression of Condensed Matter Meeting Abstracts*, 2015.

[15] Erin Gauch, James LeBlanc, and Arun Shukla. Near field underwater explosion response of polyurea coated composite cylinders. *Composite Structures*, 202:836–852, 2018.

[16] James LeBlanc and Arun Shukla. Response of polyurea-coated flat composite plates to underwater explosive loading. *Journal of Composite Materials*, 49(8):965–980, 2015.

[17] Hansohl Cho, Renaud G Rinaldi, and Mary C Boyce. Constitutive modeling of the rate-dependent resilient and dissipative large deformation behavior of a segmented copolymer polyurea. *Soft Matter*, 9(27):6319–6330, 2013.

[18] AV Amirkhizi, J Isaacs, J McGee, and S Nemat-Nasser. An experimentally-based viscoelastic constitutive model for polyurea, including pressure and temperature effects. *Philosophical magazine*, 86(36):5847–5866, 2006.

[19] Rodney J Clifton, Xinjie Wang, and Tong Jiao. A physically-based, quasilinear viscoelasticity model for the dynamic response of polyurea. *Journal of the Mechanics and Physics of Solids*, 93:8–15, 2016.

[20] Kevin Wang, Arthur Rallu, J-F Gerbeau, and Charbel Farhat. Algorithms for interface treatment and load computation in embedded boundary methods for fluid and fluid–structure interaction problems. *International Journal for Numerical Methods in Fluids*, 67(9):1175–1206, 2011.

[21] Charbel Farhat, Arthur Rallu, and Sriram Shankaran. A higher-order generalized ghost fluid method for the poor for the three-dimensional two-phase flow computation of underwater implosions. *Journal of Computational Physics*, 227(16):7674–7700, 2008.

[22] C Farhat, A Rallu, K Wang, and T Belytschko. Robust and provably second-order explicit–explicit and implicit–explicit staggered time-integrators for highly non-linear compressible fluid–structure interaction problems. *International Journal for Numerical Methods in Engineering*, 84(1):73–107, 2010.

[23] Kevin Wang, J Grétarsson, A Main, and C Farhat. Computational algorithms for tracking dynamic fluid–structure interfaces in embedded boundary methods. *International Journal for Numerical Methods in Fluids*, 70(4):515–535, 2012.

[24] Kevin Wang, Jon Gretarsson, Alex Main, and Charbel Farhat. Computational algorithms for tracking dynamic fluid-structure interfaces in embedded/immersed boundary methods. In *20th AIAA Computational Fluid Dynamics Conference*, page 3385, 2011.

[25] Alex Main and Charbel Farhat. A second-order time-accurate implicit finite volume method with exact two-phase riemann problems for compressible multi-phase fluid and fluid–structure problems. *Journal of Computational Physics*, 258:613–633, 2014.

[26] Charbel Farhat, Jean-FréDéRic Gerbeau, and Arthur Rallu. Fiver: A finite volume method based on exact two-phase riemann problems and sparse grids for multi-material flows with large density jumps. *Journal of Computational Physics*, 231(19):6360–6379, 2012.

[27] Alex Main, Xianyi Zeng, Philip Avery, and Charbel Farhat. An enhanced fiver method for multi-material flow problems with second-order convergence rate. *Journal of Computational Physics*, 329:141–172, 2017.

[28] Daniel Z Huang, Dante De Santis, and Charbel Farhat. A family of position-and orientation-independent embedded boundary methods for viscous flow and fluid–structure interaction problems. *Journal of Computational Physics*, 365:74–104, 2018.

[29] C Farhat, KG Wang, A Main, Stelios Kyriakides, L-H Lee, Krishnaswa Ravi-Chandar, and T Belytschko. Dynamic implosion of underwater cylindrical shells: experiments and computations. *International Journal of Solids and Structures*, 50(19):2943–2961, 2013.

[30] Kevin G Wang, Patrick Lea, Alex Main, Owen McGarity, and Charbel Farhat. Predictive simulation of underwater implosion: Coupling multi-material compressible fluids with cracking structures. In *ASME 2014 33rd International Conference on Ocean, Offshore and Arctic Engineering*, pages V08AT06A028–V08AT06A028. American Society of Mechanical Engineers, 2014.

[31] KG Wang, P Lea, and C Farhat. A computational framework for the simulation of high-speed multi-material fluid–structure interaction problems with dynamic fracture. *International Journal for Numerical Methods in Engineering*, 104(7):585–623, 2015.

[32] Patrick D Lea, Charbel Farhat, and Kevin G Wang. A fluid-structure coupled computational framework for fluid-induced failure and fracture. In *ASME 2015 34th International Conference on Ocean, Offshore and Arctic Engineering*. American Society of Mechanical Engineers Digital Collection, 2015.

[33] Shunxiang Cao, Ying Zhang, Defei Liao, Pei Zhong, and Kevin G Wang. Assessing the effect of lithotripter focal width on the fracture potential of stones in shockwave lithotripsy. *The Journal of the Acoustical Society of America*, 141(5):3718–3718, 2017.

[34] Kevin G Wang. Multiphase fluid-solid coupled analysis of shock-bubble-stone interaction in shockwave lithotripsy. *International journal for numerical methods in biomedical engineering*, 33(10):e2855, 2017.

[35] Shunxiang Cao, Ying Zhang, Defei Liao, Pei Zhong, and Kevin G Wang. Shock-induced damage and dynamic fracture in cylindrical bodies submerged in liquid. *International Journal of Solids and Structures*, 169:55–71, 2019.

[36] Howard Chung, Shunxiang Cao, Michael Philen, Philip S Beran, and Kevin G Wang. Cfd-csd coupled analysis of underwater propulsion using a biomimetic fin-and-joint system. *Computers & Fluids*, 172:54–66, 2018.

[37] Daniel Z Huang, Philip Avery, Charbel Farhat, Jason Rabinovitch, Armen Derkevorkian, and Lee D Peterson. Modeling, simulation and validation of supersonic parachute inflation dynamics during mars landing. In *AIAA Scitech 2020 Forum*, page 0313, 2020.

[38] Robert Hugh Cole. *Underwater explosions*. Dover Publications, 1965.

[39] Michael M Swisdak Jr. Explosion effects and properties. part ii. explosion effects in water. Technical report, Naval Surface Weapons Center White Oak Lab, Silver Spring, MD, 1978.

[40] SM Goh, MN Charalambides, and JG Williams. Determination of the constitutive constants of non-linear viscoelastic materials. *Mechanics of Time-Dependent Materials*, 8(3):255–268, 2004.